Optics Letters

Light-sheet microscopy in a glass capillary: feedback holographic control for illumination beam correction

Tobias Meinert, Benjamin Alexander Gutwein, and Alexander Rohrbach*

Laboratory for Bio- and Nano-Photonics, Department of Microsystem Engineering (IMTEK), University of Freiburg, Freiburg, Germany
**Corresponding author: rohrbach@imtek.de*

Received 29 September 2016; revised 15 December 2016; accepted 15 December 2016; posted 16 December 2016 (Doc. ID 277734); published 12 January 2017

Light-sheet microscopy enables fast 3D, high-contrast imaging in biology and colloidal sciences. Recently, the controlled transport of living embryos or small colloids through stable glass capillaries is manifold interesting. Although they hardly impair the sample, glass capillaries spoil the image by generating significant aberrations of the illumination and detection light. Here, we analyze the deflection of illuminating Bessel beams at the capillary by k-spectral shifting, and correct for it by a beam deflector. Using cylindrical lenses for astigmatism compensation on the detection side, we demonstrate 3D line-confocal imaging inside a glass capillary over an axial range of ±400 μm.

OCIS codes: (180.6900) Three-dimensional microscopy; (110.1085) Adaptive imaging; (090.1000) Aberration compensation; (110.2970) Image detection systems; (230.6120) Spatial light modulators.

https://doi.org/10.1364/OL.42.000350

Light-sheet microscopy (LSM) has become the method of choice for long-term 3D imaging with high resolution in space and time to investigate the 3D dynamics of individual cells [1]. If isolated sub-volumes can be generated, highly dynamic processes such as the coupled motion of colloids and bacteria in constrained diffusion volumes, for example, capillaries [2], can be investigated by LSM [3].

The standard embedding of biological object in agarose cylinders requires agarose concentrations of 1–1.5% to ensure sufficient mechanical stability, but results in high gel viscosities and thus hampers growth and movements of living specimens [4]. Low-refracting fluorinated ethylene propylene tubes allow the isolation of volumes for cost-effective usage of expensive media enabling imaging of stem cell and embryonic development [4]. Large enough glass capillaries on the other side are the most prominent tool for sample handling in biotechnology because of their better mechanical and optical stability, their sterility, and their ability for surface functionalization. Their usage in LSM would facilitate and accelerate many processing steps. Examples are the defined medium exchange through connections at the capillary ends [5–7] or the usage of higher refracting clearing fluids. The optical aberrations, caused by the glass sample holder or the sample itself [8–10], can be corrected by adaptive optics on the detection side [11,12]. Recently, adaptive optics was also applied in the illumination path [13], but the phase correction is only valid for one point in the 3D sample.

Here we show a simple approach to enable LSM inside a glass capillary: while in detection direction, two cylindrical lenses were used for astigmatism compensation, we use Bessel beams in the illumination arm and record their annular k-spectrum, which shifts upon refraction at the capillary. This effect allows an easy analysis and efficient correction of the aberrated wavefront. As a test sample, we imaged fluorescing beads as approximate point sources for an objective system analysis, which is not possible by using complex biological specimens.

Figure 1 shows a sketch of our Bessel beam LSM setup, which has been explained in more detail elsewhere [14].

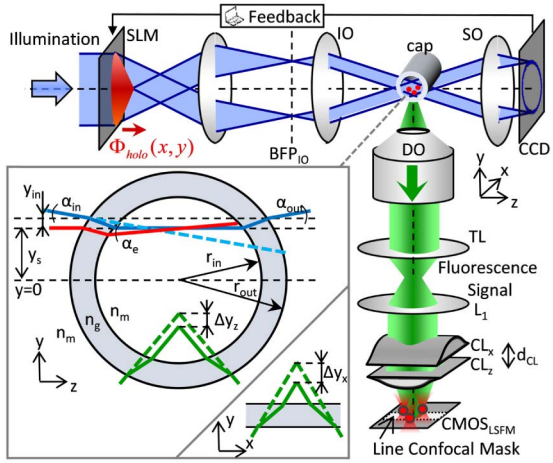

Fig. 1. Light-sheet setup with a two-fold aberration correction. In the illumination path, a SLM (Pluto NIR II, Holoeye) enables feedbacked phase correction. A pair of cylindrical lenses in the detection path (CL_x, CL_z) compensates for astigmatism caused by the capillary (cap) used as a sample holder. Inset: the illumination beam needs to be corrected such that it propagates horizontally inside the capillary (blue solid line, angles $\alpha_{in} = -\alpha_{out}$).

The fluorescence light emitted by the object is collected by the detection objective, oriented 90° to the illumination objective.

In the detection path, light transmission through the capillary causes mainly astigmatism. We corrected for this by an additional 4f-imaging system (Fig. 1), consisting of an achromatic lens (L_1, $f_1 = 120$ mm) and a pair of cylindrical lenses (CL_x, CL_z, $f_x = f_z = 125$ mm) in a defined distance $d_{CL} = 9.6$ mm, where the focal lines of the cylindrical lenses (CL) have to be 90° to each other.

In the illumination path, tilt and defocus are corrected by wavefront shaping via a spatial light modulator (SLM), where the conical phase of the Bessel beam is combined with a linear phase for beam tilting ($\phi_{holo}(x, y, \alpha_{in})$). The shift of the ring-like angular spectrum of the illumination beam was recorded through a scattering objective and a CCD (Fig. 1), used as a feedback signal for the SLM to correct the angle of incidence α_{in}.

Classical adaptive optics based on a wavefront sensor and a deformable mirror have been used in the detection path of LSMs to improve image quality [11,12]. If a glass capillary is used as a sample holder, the main sources of image degradation are defocus and astigmatism [11]. Defocus can be corrected by shifting the illumination light sheet. In order to correct only for astigmatism, a costly deformable mirror is not necessary. Astigmatism can be corrected via a 4f-system with the second lens replaced by a pair of CLs in an axial distance d_{CL} and with a compensating phase $\phi_{CL}(x, z) = \sqrt{(f_x^2 - x^2)} + \sqrt{(f_z^2 - z^2)}$. A point imaged through two orthogonal CLs generates two focal lines in the x- and z-directions at different axial positions in a distance d_{CL}. Hence, two CLs generate astigmatism or compensate for it, if d_{CL} is chosen accordingly.

d_{CL} is estimated as follows: the capillary is not curved in the x-direction, such that the shift of the focal line $\Delta y_x = t \cdot (n_m/n_g - 1)$ does not depend on the capillary position y_s, but on the wall thickness $t = r_{out} - r_{in}$ (inset Fig. 1). r_{out} and r_{in} are the outer and inner radii of the capillary, and n_g and n_m are the refractive indices of the capillary and the media, respectively. A positive value of Δy indicates a shift in the positive y-direction. In the z-direction, the capillary acts like a CL, with a focal length $f_{cap} = r_{out} r_{in}/[t \cdot (n_m/n_g - 1)]$ and a principal plane in the center of the capillary. Thus, the shift of the focal line in the z-direction Δy_z (inset in Fig. 1) depends on the position of the capillary center y_s relative to the focal plane (without capillary), and is given by $\Delta y_z(y_s) = y_s - (f_{cap}^{-1} + y_s^{-1})^{-1} = y_s^2/(y_s + f_{cap}) \approx y_s^2/(f_{cap})$. The approximation $|y_s| \ll |f_c|$ is valid for all cases considered in this Letter. Note that Δy_z is negative, if f_c is negative, which is true as long as $n_m < n_g$. d_{CL} is given by the distance of the focal lines scaled by the longitudinal magnification $M_{det}^2 = 20^2$ of the detection system:

$$d_{CL} = M_{det}^2 \cdot (\Delta y_x - \Delta y_z(y_s)) \approx M_{det}^2 \Delta y_x (1 - y_s^2/(r_{out} r_{in})). \quad \textbf{(1)}$$

To validate these theoretical considerations, we measured the detection point spread function (PSF) of our LSM. Therefore, we embedded fluorescent 0.4 μm beads in 0.5% agarose gel ($n_m = 1.33$) inside a glass capillary and scanned the capillary in the y-direction through the focal plane. To ensure that the detection PSF $h_{det}(\mathbf{r})$ and not the system PSF ($h_{det} \cdot h_{ill}$, with h_{ill} being the illumination light sheet) is imaged, we kept the relative position of the light sheet in the object constant. This was possible by adjusting the y-position of the illumination beam via the SLM.

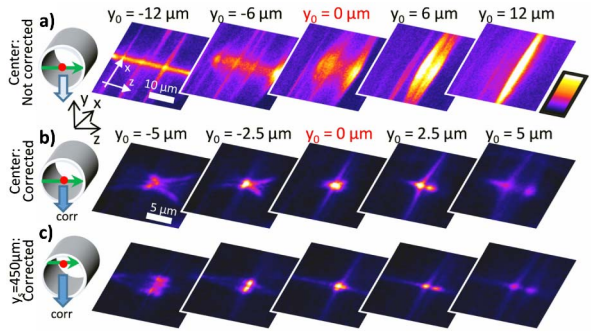

Fig. 2. Single bead imaging through a capillary. The capillary shifts the focus in the x- and z-directions differently. This results in strong astigmatism, as illustrated by the five images in (a). A pair of crossed CLs compensates for the astigmatism. The detection PSFs $h_{det}(x, y_0, z)$ depicted in (b) show that this correction works well in the center of the capillary. (c) Similar detection PSF at $y_s = 450$ μm is measured without adapting d_{CL}.

Figure 2(a) shows the PSF without correction. Strong astigmatism effects are visible. The focal lines in the x- and z-directions are axially displaced by more than 20 μm. This fits well with the theoretical estimate of $\Delta y_x - \Delta y_z(y_s = 0) = \Delta y_x = 24$ μm, based on the used capillary with $r_{out} = 850$ μm, $r_{in} = 600$ μm, and $n_g = 1.47$.

To compensate for the astigmatism, d_{CL} was set to roughly $M_{det}^2 \times 24$ μm $= 9.6$ cm. Figure 2(b) shows that compensation works well in the center of the capillary. The further the beads are from the capillary center ($|y_s| > 0$), the stronger is Δy_z, and the weaker is the astigmatism. Without an adjustment of d_{CL}, an overcompensation of the astigmatism will occur, as slightly visible in Fig. 2(c).

It should be noted that the shape of the PSF, distorted by spherical aberrations and astigmatism, is partly compensated for by confocal line detection.

The illuminating Bessel beam is formed via a hologram given by

$$\phi_{holo}(x, y) = T(x, \delta y) \cdot \exp\left(-ik_r \sqrt{x^2 + \delta y^2}\right) \cdot \exp(-ik_y y). \quad \textbf{(2)}$$

Here $T(x, \delta y)$ with $\delta y = y - y'_{in}$ is the annular amplitude modulation of the hologram. The inner and outer radii of the annulus determine the axial beam position and length. The slope of the conical phase defines the numerical aperture of the beam NA $= n_m \sin(k_r/(k \cdot M_{ill}))$ with a wave number $k = 2\pi/\lambda$ ($\lambda = 491$ nm) and magnification of the illumination system $M_{ill} = 40$ [14]. The shifts in the Fourier space and in real space, k_y and y'_{in}, are used for the beam correction. The former defines the incident beam position $y_{in} = y'_{in} \cdot M_{ill}$, while the latter sets the beam tilt $\alpha_{in} \approx k_y/(k \cdot M_{ill})$.

The goal of the correction is to make the beam propagating parallel to the z-axis ($\alpha_e = 0$) in the focal plane of the microscope ($y_e = 0$). The corrected incident beam angle α_{cor} and position y_{cor} can be determined by geometrical optics. Note that y_{cor} depends on both y_{in} (as depicted in Fig. 1) and on y_s, which changes the focal plane and the entry point of the illumination beam on the capillary due to the angle correction.

Although the correction parameters can be theoretically predicted, a feedbacked correction is more robust. Due to the symmetry of the capillary, one finds $\alpha_e = 0$, if the angle of incidence α_{in} and the exit angle α_{out} only change their sign (inset

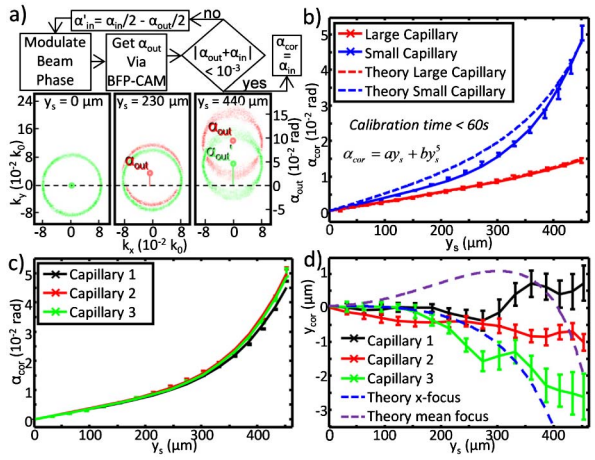

Fig. 3. Illumination beam correction. (a) Flow chart of the angle correction algorithm and BFP images of the deflected Bessel beam (corrected in green; uncorrected in red). (b) Correction angle α_{in} is adjusted for each capillary position such that the light sheet is horizontal inside the capillary (two different sizes). The position dependent correction angle (c) and the defocus between the light-sheet and the focal plane after angle correction (d) is plotted for different capillaries from the same batch. The error bars indicate the standard deviation of three measurements with the same capillary.

of Fig. 1). Based on this, we developed a quickly converging algorithm for angle correction. The flowchart of the algorithm is shown in Fig. 3(a). First, we set the initial incident angle by modulating the beam phase via the SLM and determine the exit angle in the back focal plane (BFP). If α_{in} and $-\alpha_{out}$ vary by more than 10^{-3} rad, a new value for α_{in} is estimated. If $\alpha_{in} \approx -\alpha_{out}$, the algorithm has found the corrected incident angle α_{cor}.

Since a Bessel beam is used for illumination, the CCD camera in the BFP shows a ring spectrum, which shifts by k_y depending on the beam deflection. The ring center represents α_{out} [8] and is easily obtained by fitting a circle to the ring. In order to test the fitting, even under scattering conditions, we filled the capillary with 0.4 µm small polystyrene beads in 0.5% agarose. The rings depicted in Fig. 3(a) show that circle fitting is easily possible for bead concentrations of 0.017 vol%, but even stronger scattering should not cause significant problems.

Figure 3(b) depicts how α_{cor} increases with the position y_s of two different capillaries (blue, $r_{out} = 850$ µm and $r_{in} = 600$ µm; red, $r_{out} = 1250$ µm and $r_{in} = 950$ µm). The calibration processes start at $y_s = 0$ with initial $\alpha_{in} = 0$. The initial α_{in} of the next y_s position is given by α_{cor} of the previous y_s. This way a maximum of two iterations ($\approx 2 \times 0.2$ sec) is necessary. Both curves can be well approximated by $ay_s + by_s^5$. This allows a strong reduction of the number of calibration points and, in conjunction with the low number of iterations, enables angle calibration for all capillary positions in less than one minute. Note that calibration only relies on coherently scattered light and, thus, requires very low intensities, which do not bleach the sample.

Figure 3(c) shows that the variation for the angle correction is quite small for different capillaries from the same batch. This is in contrast to the defocus y_{cor} displayed in Fig. 3(d). The course of y_{cor}, depending on y_s, is different for each capillary, which we attribute to the non-constant wall thicknesses of the capillaries. The theoretical prediction of y_{cor} given by the dashed lines considers the change of the astigmatism with y_s. For Fig. 3(d), y_{cor} has been determined by imaging the illumination beam in fluorescein and finding the value of y_{in}, which generates the highest contrast of the Bessel ring frequency. Since these frequencies are present only in the x-direction, the results have to be compared to the blue dashed line, which refers to the plane with the highest focusing in the x-direction. The purple line, which refers to the focal plane with the best compromise of x- and z-focusing, predicts $|y_{cor}| < 1$ µm for $y_s < 400$ µm. Hence, for capillaries with constant and well-defined wall thicknesses, one can assume $y_{cor} = 0$.

However, we were able to capture 3D image stacks in capillaries with non-constant wall thicknesses which require theoretically non-predictable and non-negligible y_{cor}. We defined y_{cor} by imaging the object at some scan positions y_s and finding y_{in} with the sharpest image by visual impression. For all other y_s-positions, y_{cor} has been determined by linear regression.

The quality of a confocal image $I(\mathbf{r}) = I(\mathbf{r}, y_{in}, \alpha_{in}, y_s, d_{CL})$ [15] acquired from an object inside a glass capillary at position y_s depends on the position y_{in} and tilt α_{in} of the incident illumination beam h_{ill}. It also depends on the detection PSF $h_{det}(\mathbf{r}, y_s, d_{CL})$, which is strongly affected by the CL distance d_{CL}, such that the image formation is expressed as follows:

$$I(x, y_0, z) = (h_{ill}(x, y - (\alpha_e z' + y_e), z) \cdot h_{det}(\mathbf{r}, y_s, d_{CL})) * c(\mathbf{r})|_{y0}. \quad (3)$$

The illumination beam with intensity $h_{ill}(\mathbf{r}, y_{in}, \alpha_{in})$ is tilted by α_e and depends on the y-shift $y' = \alpha_e \cdot z' + y_e$ with defocus y_e. z' differs from z, since the system PSF is no longer shift invariant. $c(\mathbf{r}) \approx c_0 \sum_j \delta(\mathbf{r} - \mathbf{r}_j)$ describes the fluorophore distribution of the object, which is a random distribution of small beads in our case. For such point emitters, the image spectrum $\tilde{I}(k_x, y_0, k_z) = |\mathrm{FT}_{xy}[I(x, y_0, z)]|$ can be approximated by the modulation transfer function $\mathrm{MTF}(k_x, k_z) \approx \tilde{I}(k_x, k_z) = |\mathrm{FT}[h_{ill}(\mathbf{r}, \mathbf{r}') \cdot h_{det}(\mathbf{r})]|$.

As shown by the experimental results in Fig. 2, the adaption of the astigmatism correction in the detection path is not crucial, i.e., y_s hardly affects d_{CL}. Thus, the adapted phase correction of the illumination light via the SLM enables fully automated 3D imaging after a calibration run (described above). Remarkably, the same calibration procedure can be performed if a beam deflecting object is inside the capillary.

For a quantitative comparison of corrected and uncorrected images, each slice in the stack was imaged with and without beam correction, before the object was moved to the next y-position. However, if no comparison to uncorrected imaging is required, it is not necessary to update the hologram for each y_s-position. Since the angle correction is limited to 3°, only 60 hologram updates are required for a sufficient correction step size of 0.05°.

We first acquired images in the center of the capillary and then moved the object downward in steps of 0.7 µm. Figure 4 shows an image in the center of the capillary, where no illumination correction is needed, and an image at $y_s = 450$ µm with and without correction. The images were acquired in confocal mode with a slit width of 1.3 µm [15]. For illumination, we used a Bessel beam with $\mathrm{NA}_{ill} = 0.08$. All images are from 0.4 µm fluorescent PS beads at a concentration of 0.017 vol%.

Left and right of the images $I(x, y_0, z)$, the corresponding image spectra $|\mathrm{FT}[I(x, y_0, z)]|$ are shown in logarithmic scale. Obviously, the best image quality is achieved in the center of the capillary, such that the Fourier spectra are broadest (see the

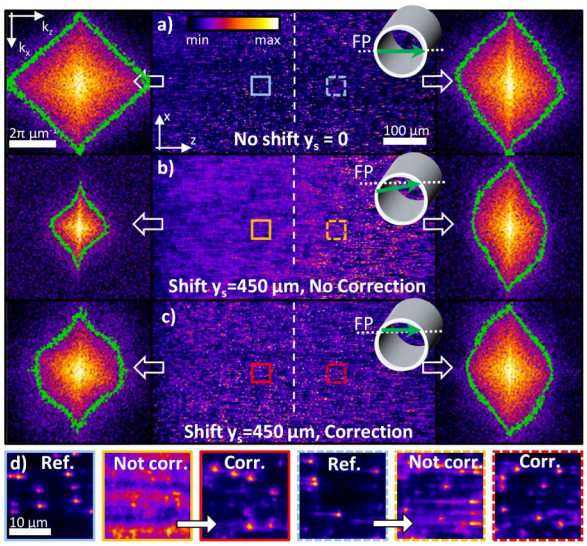

Fig. 4. Line-confocal images of fluorescent 0.4 µm beads inside a glass capillary. (a) Center of the capillary is in the focal plane ($y_s = 0$), no correction is needed. (b) Displacing the capillary in the y-direction ($y_s = 450$ µm) leads to a tilted illumination and a strong z dependent defocus. (c) Illumination tilt is corrected by the SLM. The corresponding Fourier spectra are depicted to the left and right of the bead images. (d) Magnifications of the ROIs.

green iso-intensity line at 20%). Shifting the capillary downward in the y-direction leads to a tilt of the illumination beam relative to the focal plane (insets in Fig. 4), resulting in a z-dependent defocus ($\alpha_e \cdot z' + y_e$). This leads to a larger overlap between the tilted $h_{\mathrm{ill}}(\mathbf{r})$ and $h_{\mathrm{det}}(\mathbf{r})$, which becomes broader along y (defocus area). The increased system PSF results in a reduced spectral width as visible in Fig. 4(b).

A beam correction, through control of the parameters y_{in} and α_{in}, compensates for this defocus and increases the image quality strongly. Figure 4(c) reveals that especially on the left side the spectral width and thus the resolution is roughly doubled. The image quality is not as good as in the center of the capillary, since astigmatism correction in the detection path is not optimized for the outer area of the capillary. The magnifications of the regions of interest (ROIs) in Fig. 4(d) emphasize the efficiency of our correction. The diamond shape of the image spectra, the autocorrelation $\mathrm{AC}\{\mathrm{FT}[\exp(i\phi_{\mathrm{CL}}(x,z))] \cdot \exp(-if\sqrt{(k^2 - k_x^2 - k_z^2)})\}$ is caused by the non-rotational symmetric phase ϕ_{CL} generated by the crossed CLs.

We demonstrated that 3D light-sheet microscopy in a glass capillary works well, if optical corrections are applied on both the illumination and the detection sides. We used a scanned Bessel beam to generate the light sheet, which is typically used in combination with line-confocal detection. Much better than a Gaussian beam, the central lobe of the Bessel beam can be treated like a geometrical ray [8], which facilitates the correction strategy and the optical design.

To correct aberrations caused by the capillary in the detection path, a deformable mirror is not necessarily needed. Our cheap solution with two crossed CLs is suitable to compensate for the main source of the image degradation, which is astigmatism. Placing one of the lenses on a translation stage would enable automated adaption of astigmatism correction to keep the image quality constant over the whole 3D field of view.

We showed that feedbacked holographic beam shaping improves the image quality in LSM. In principle, our angle correction method can be applied to any object symmetrical to the xy-plane. The calibration process for the angle correction relies only on coherently scattered light and, thus, can be carried out at very low intensities. This prevents phototoxic effects by the aberration correction.

The SLM (Holoeye, Pluto) with 10 Hz frame rate was a bottleneck for fast imaging. However, the SLM is only used for tilt and defocus correction and can be replaced by two galvo scan-mirrors, one located in a plane conjugated to the BFP of the illumination beam for defocus correction and the other located in a plane conjugated to the focal plane of the illumination beam for tilt correction. If both mirrors are biaxial, the correction can be performed not only in the y-, but also in the x-direction. This is of interest for imaging spherical cell clusters [8], to mention one example.

Our achieved image quality will allow not only particle tracking to study fluid motion, but also should increase the image quality of more complex biological structures inside 1 mm thick capillaries. The presented method does not rely on index matching and, thus, can be adapted to any immersion media, such as clearing agents. Glass capillaries are a standard tool for sample preparation and mounting in biotechnological screening and research applications. Hence, this Letter should be of great help for future LSM applications, which cannot relinquish on the advantages of glass capillaries, but still demand for high quality 3D imaging.

Funding. Deutsche Forschungsgemeinschaft (DFG) (RO3615/4).

REFERENCES

1. B. C. Chen, W. R. Legant, K. Wang, L. Shao, D. E. Milkie, M. W. Davidson, C. Janetopoulos, X. S. Wu, J. A. Hammer, Z. Liu, B. P. English, Y. Mimori-Kiyosue, D. P. Romero, A. T. Ritter, J. Lippincott-Schwartz, L. Fritz-Laylin, R. D. Mullins, D. M. Mitchell, J. N. Bembenek, A. C. Reymann, R. Bohme, S. W. Grill, J. T. Wang, G. Seydoux, U. S. Tulu, D. P. Kiehart, and E. Betzig, Science **346**, 1257998 (2014).
2. C. Maggi, M. Paoluzzi, N. Pellicciotta, A. Lepore, L. Angelani, and R. Di Leonardo, Phys. Rev. Lett. **113**, 238303 (2014).
3. D. M. Wulstein, K. E. Regan, R. M. Robertson-Anderson, and R. McGorty, Opt. Express **24**, 20881 (2016).
4. A. Kaufmann, M. Mickoleit, M. Weber, and J. Huisken, Development **139**, 3242 (2012).
5. C. Pardo-Martin, A. Allalou, J. Medina, P. M. Eimon, C. Wählby, and M. Fatih Yanik, Nat. Commun. **4**, 1467 (2013).
6. T.-Y. Chang, C. Pardo-Martin, A. Allalou, C. Wahlby, and M. F. Yanik, Lab Chip **12**, 711 (2012).
7. T. Bruns, S. Schickinger, and H. Schneckenburger, J. Microsc. **260**, 30 (2015).
8. S. Hoda Moosavi, C. Gohn-Kreuz, and A. Rohrbach, Appl. Opt. **52**, 5835 (2013).
9. T. Meinert, O. Tietz, K. J. Palme, and A. Rohrbach, Sci. Rep. **6**, 30378 (2016).
10. D. Turaga and T. E. Holy, Biomed. Opt. Express **4**, 1654 (2013).
11. C. Bourgenot, C. D. Saunter, J. M. Taylor, J. M. Girkin, and G. D. Love, Opt. Express **20**, 13252 (2012).
12. R. Jorand, G. Le Corre, J. Andilla, A. Maandhui, C. Frongia, V. Lobjois, B. Ducommun, and C. Lorenzo, PLoS One **7**, e35795 (2012).
13. D. Wilding, P. Pozzi, O. Soloviev, G. Vdovin, and M. Verhaegen, Opt. Express **24**, 24896 (2016).
14. F. O. Fahrbach and A. Rohrbach, Opt. Express **18**, 24229 (2010).
15. F. O. Fahrbach and A. Rohrbach, Nat. Commun. **3**, 632 (2012).